Montanuniversität Leoben

Oxidation and wet etching behavior of sputtered ternary molybdenum alloy thin films

Diploma Thesis

by

Tanja Jörg

This work was done in cooperation with PLANSEE SE, within the Competence Headquarters Project E^2-Sputtertech, with financial support from the Österreichische Forschungsförderungsgesellschaft at the Chair of Functional Materials and Materials Systems, Montanuniversität Leoben, Austria.

Leoben, March 2014

Affidavit

I declare in lieu of oath, that I wrote this thesis and performed the associated research myself, using only literature cited in this volume.

Leoben, March 2014

T. Jörg

Acknowledgments

My sincere appreciation is due to Prof. Dr. Christian Mitterer, head of the Chair of Functional Materials and Materials Systems, for his guidance and encouragement and from whose knowledge and expertise I benefited so greatly.

I am grateful to my supervisor DI Anna Hofer for her valuable advice during the research and writing of this thesis.

I would like to express my gratitude to Dr. Jörg Winkler and Dr. Harald Köstenbauer from PLANSEE SE for their support and contribution to this work.

Many special thanks to all the members of the “Thin Film Group” and of the Department of Physical Metallurgy and Materials Testing, for their help whenever needed and including me in their team.

Furthermore, I am thankful to my friends, for all the emotional support they provided.

I would like to thank my parents and sister for believing in me, for their continuous love and their support in my decisions.

Finally, I want to express my gratefulness to Volker, who always stood by my side. Thank you for the countless encouragements and for always bringing a smile to my face.

Contents

1 **Introduction** ... 1

2 **Theoretical aspects** ... 2

2.1 Sputter deposition ... 2

2.1.1 Magnetron sputtering ... 3

2.2 Thin film structure ... 5

2.2.1 Nucleation and growth ... 5

2.2.2 Structure zone models ... 6

2.3 Oxidation ... 8

2.3.1 Fundamentals of oxidation ... 8

2.3.2 Oxidation behavior of Mo and Mo alloys ... 11

2.4 Wet etching ... 12

2.4.1 Wet etching of Mo and Al ... 13

Bibliography ... 15

3 **Manuscript** ... 18

Appendix ... 31

1 Introduction

Sputtered molybdenum (Mo) thin films are used in thin film transistor liquid crystal displays (TFT-LCD) as conducting materials. Their low electrical resistance and easy chemical patterning make them an excellent material for source/drain electrodes and data bus-lines. Furthermore, Mo thin films are used as bottom and capping layers in the gate metallization of TFTs, due to their good adhesion on glass and low contact resistance to silicon and indium tin oxide [1]. They also serve as diffusion barrier, since Mo exhibits a high melting point and very low diffusion coefficients [2,3].

Since annealing treatments are used in TFT-LCD processing [4], these films have to withstand thermal exposure without deterioration of their properties. However, exposure of molybdenum thin films above 300°C in ambient atmosphere results in surface oxidation, leading to the formation of colored oxide films, as shown in Fig. 1 [5,6]. Alloying of Mo thin films has been suggested to improve their oxidation resistance [7]. For example, Park et al. have reported that Ti is corrosion resistant in oxidizing atmospheres and that alloying Ti to Mo leads to the formation of a passivation layer [8]. However, Ti cannot be dissolved in phosphoric, acetic, nitric acid solutions (PAN), which is a key process step used for patterning in the production of TFT materials [9].

To overcome this problem, ternary Mo-X-Al (X=Ti or Mg) alloys are synthesized by sputter deposition, since Al is known for its superior oxidation resistance and good wet etching behavior in PAN [9]. The aim of this work is to study the microstructure, electrical properties, oxidation and wet etching behavior of these ternary Mo-X-Al and reference Mo-Ti-Ni films. The first part of the thesis gives a theoretical overview of the sputter deposition process and covers the fundamental aspects of oxidation and wet etching. The main scientific output of this work is presented as a manuscript in the second part of the thesis. Additional data and a comparison between the different Mo-X-Y alloys are given in the appendix.

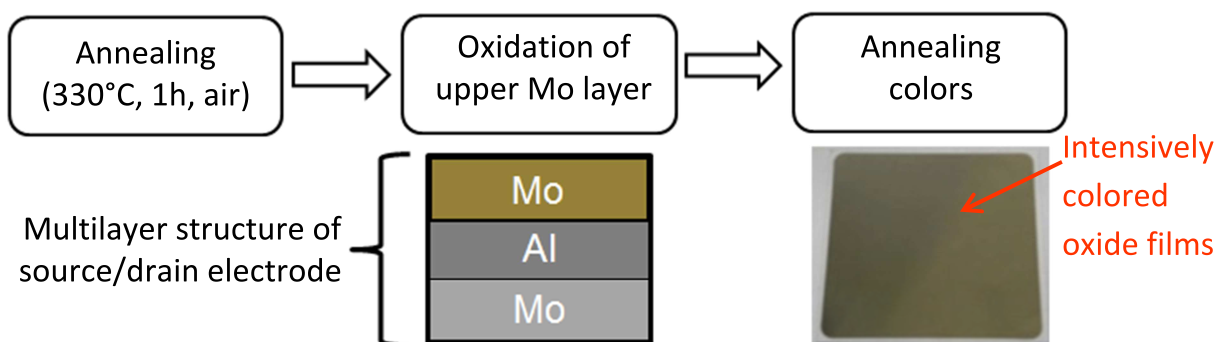

Fig. 1. Effect of the annealing treatment on sputtered Mo thin films.

2 Theoretical aspects

2.1 Sputter deposition

The sputtering process is a thin film deposition method, which belongs to the physical vapor deposition (PVD) techniques. Sputtering was first described in 1852 by W.R. Grove, who noticed metal deposits sputtered from a glow discharge of a silver cathode. At first, sputtering was mostly used to deposit metal films for mirrors. However, it was not until the 1970s, that the development of magnetron sputtering allowed higher deposition rates and therefore opened the market for a broader range of applications [10]. Nowadays, sputter deposition is one of the most important thin film deposition techniques and plays a key role in the fabrication of microelectronics and semiconductor devices. Basically, any solid material can be deposited through sputtering, including elements, alloys, or compounds [11].

Sputtering takes place in the presence of a glow discharge plasma, which is characterized as partially ionized low-pressure gas. A plasma consists of electrically neutral and charged particles such as atoms, ions, electrons, and is overall electrically neutral [12].

Sputter deposition is a process in which atoms are physically vaporized from a solid surface (target) by energetic particles. The incident particles are usually gaseous ions (e.g. Ar^+), accelerated from a plasma towards the target surface. Fig. 2.1 shows incident ions bombarding the target and ejecting atoms from the surface by momentum transfer. The energy of incident ions needs to be high enough to create collision cascades, in which the primary knock-on atoms cause a series of collisions and eventually lead to the ejection of a surface atom. The ratio of ejected atoms from the target surface to the incident ion is called sputtering yield. The sputtering yield depends strongly on the mass of incident and ejected atoms as well as on the energy transferred by the collision [11].

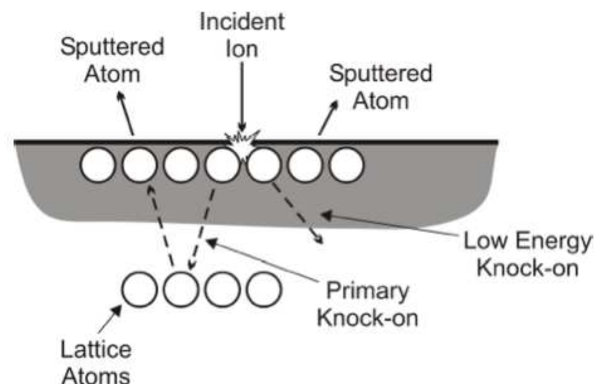

Fig. 2.1 Momentum transfer processes during sputtering under the influence of incident ions [13].

2.1.1 Magnetron sputtering

Magnetron sputtering has become the most common process for growing thin films by sputter deposition, used in nearly 95% of all sputtering applications [14].

A direct current (dc) magnetron sputtering system, which basically consists of two electrodes, is shown schematically in Fig. 2.2. The negative potential of the dc power supply is applied to the cathode or target to generate a glow discharge (plasma). Positive ions of the plasma are accelerated towards the target, knocking off or sputtering atoms from the target surface. In a magnetron-based system this process is enhanced by positioning permanent magnets behind the target inducing a strong magnetic field (see Fig. 2.2). By employing this magnetic field, the secondary electrons produced by ion bombardment circle around the magnetic flux lines and stay near the target. Thus, the ionization efficiency is enhanced, resulting in a denser plasma that can be sustained at a lower working gas pressure. The magnetic field only affects electrons but not ions, since they exhibit a higher mass than electrons [15,16].

However, the strong confinement of the plasma near the target surface leads to high sputtering rates in the area of the drift loops. As a consequence, the erosion of the target material is localized and non-uniform [11].

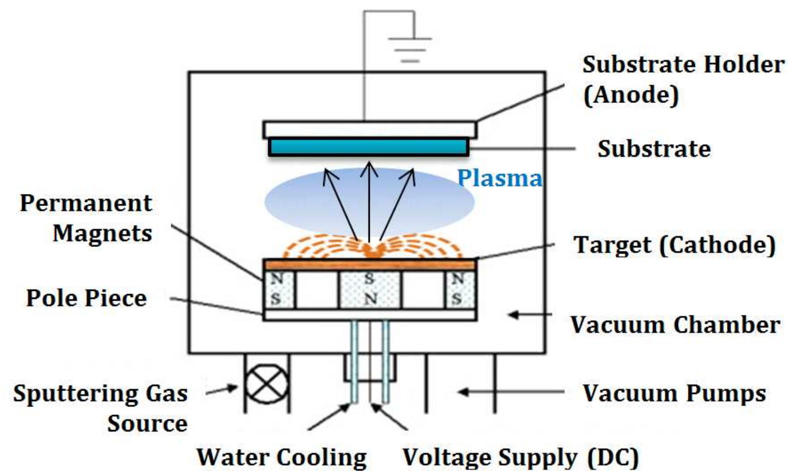

Fig. 2.2 Schematic of a d.c magnetron sputtering system after [17].

The planar magnetron is the most frequently used magnetron source and available for a large choice of target geometries, e.g. square, rectangular or circular. A typical configuration of a circular target is shown in Fig. 2.3, where the magnetic field lines have a circular symmetry and form an ideal loop between the inner and outer magnets. As a result of the non-uniform plasma distribution, the area of erosion is a closed circle [15,18].

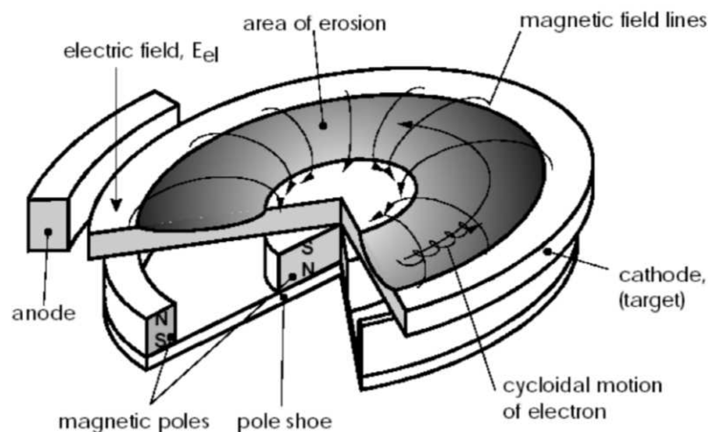

Fig. 2.3 Schematic illustration of a planar circular magnetron configuration [19].

Since the inner and outer magnets are perfectly balanced, this type of magnetron is called conventional balanced magnetron (CBM). One disadvantage of the CBM is that the plasma is concentrated in the target region and therefore the ion bombardment of the substrate region is minimal (see Fig. 2.4a). The low substrate ion current limits the performance of the film, making it difficult to deposit a dense, high quality coating. This obstacle can be overcome by enhancing either outer or inner magnet, so that the magnetic field lines are no longer constrained between inner and outer magnets. This magnetic field configuration is referred to as unbalanced magnetron (UBM). In an UBM, the magnetic field lines reach the substrate, as illustrated in Fig. 2.4b. As a consequence, some electrons are able to follow the magnetic field lines towards the substrate. Hence, the ionization rate near the substrate is increased, resulting in a higher ion bombardment of the surface, which improves the film structure and properties [20,21].

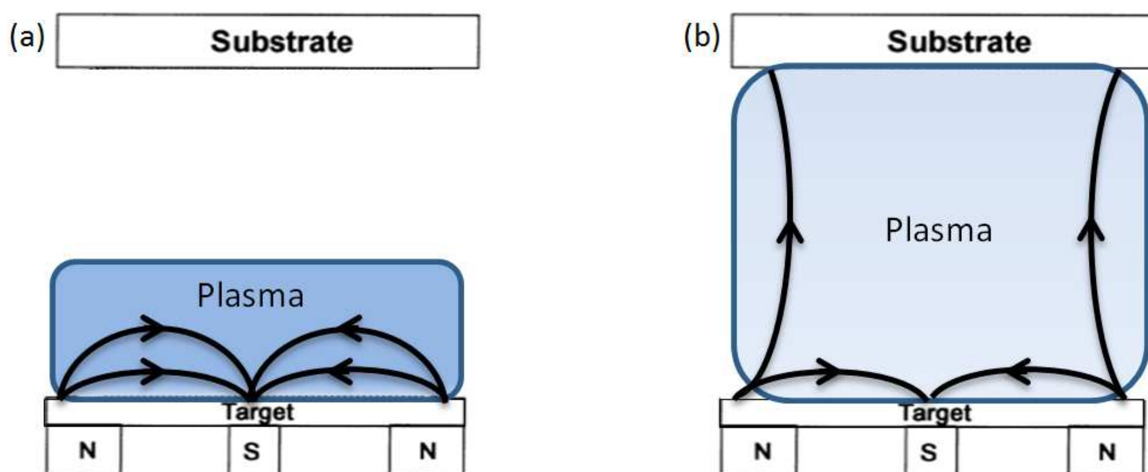

Fig. 2.4 Schematic representation of the magnetic configuration in (a) CBM and (b) UBM after [20].

2.2 Thin film structure

Sputtering is a non-equilibrium process; consequently thin films prepared by sputter deposition exhibit quite different microstructures than bulk materials [22]. This difference can be better understood by looking at the structural evolution during film growth.

2.2.1 Nucleation and growth

The initial stage of film formation is the condensation and adsorption of the sputtered atoms on the substrate surface. Depending on the energy transfer with the surface, the atoms are either reflected immediately or become loosely bonded adatoms. Diffusion processes on the surface enable the interaction of these adatoms, resulting in an assembly of metastable clusters. These small clusters are still mobile and grow by assembling with other clusters until they reach a critical size and become stable nuclei (see Fig. 2.5). This process is referred to as nucleation. The stable nuclei continue to grow and finally form a continuous film [11,23]. Depending on the interaction between the adatoms and the substrate surface, three primary growth modes can be observed. When the adatoms are stronger bound to each other than to the substrate, 3D or Volmer–Weber growth occurs. During the early stage of this mode, stable nuclei grow in three dimensions and form islands by incorporating atoms from the vapor phase or surface diffusion. Thus, the islands are increased in size, whereas the density of the islands saturates. Finally, the islands merge together and create a continuous film. This process is called coalescence and driven is by minimization of surface and interface energy. For instance, this growth mode is observed in the deposition of a metal on an insulator substrate [12].

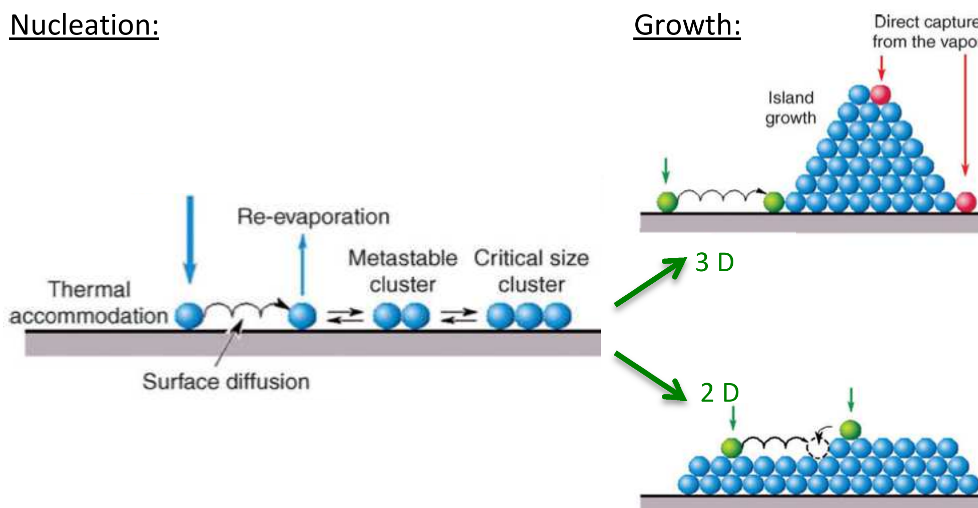

Fig. 2.5 Schematic processes of nucleation and 3D and 2D film growth after [18].

If the adatoms bond stronger to the substrate than to each other, stable nuclei grow in two dimensions and form a planar layer. Accordingly, this growth mechanism is known as 2D or Frank-Van der Merwe growth and the dominant mechanism in the epitaxial growth of semiconductor films. The third growth mode is a combination of the two previous ones and called Stranski-Krastanov mode. The characteristic of this mode is the transition from initial 2D layer growth to 3D island growth [12].

2.2.2 Structure zone models

The microstructure of thin films strongly depends on the process conditions during film growth. Accordingly, various structure zone models (SZMs) based on experimental results have been developed to predict those dependencies. It has been reported by Barna and Adamik [24], that the two most important parameters influencing the structure evolution in polycrystalline film growth are substrate temperature and the amount of incorporated impurities. They proposed two types of structure zone models, a basic and real SZM. The basic SZM describes the microstructure evolution of pure films as a function of the temperature. The distinct morphological zones of this model are shown in Fig. 2.6.

The primary feature of Zone I is the random crystal growth. The film exhibits a fine fibrous structure, in which the crystalline fibers preserve the random orientation of the nuclei. Due to the low substrate temperature, no bulk diffusion and almost no surface diffusion take place. In Zone T, competitive growth of the different oriented crystals occurs. A transition in morphology with increasing thickness is observed. Near the substrate region, the structure is composed of fine randomly oriented fibers, which emerge into V-shaped columns as thickness increases. The columns with kinetically favored orientation overgrow the others, resulting in an increased preferential orientation. Surface diffusion is activated, whereas grain boundary migration is very limited. The main characteristic of Zone II is development of a restructuring growth texture. Due to the increased grain boundary mobility, coalescence and grain coarsening occur. The film consists of single-crystalline columns and is homogeneous over its whole thickness. The columns broaden as the temperature is further increased [24,25,26].

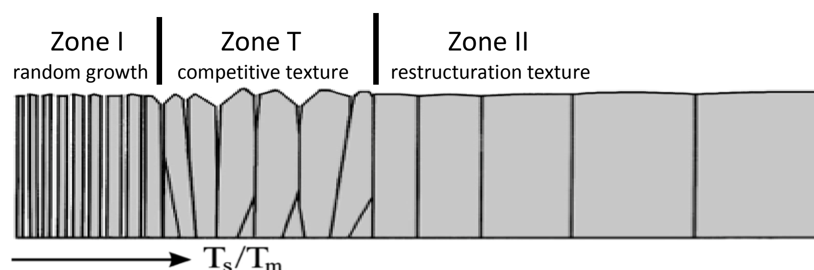

Fig. 2.6 Schematic illustration of the basic structure zone model after [27].

Since the presence of impurities during the deposition process is unavoidable, Barna and Adamik established the concept of real structure zone models, considering the effect of co-deposited additives such as oxygen or carbon. This model is illustrated in Fig. 2.7 demonstrating the influence of low (C_{imp} < 0.5 %), medium (C_{imp} ≈ 1 %) and high (C_{imp} > 10 %) impurity content on the microstructure [24].

At low temperatures (Zone I), the segregation of impurities is limited and they are incorporated into the forming fibrous structure. Consequently, the addition of impurities to the system does not affect the evolving microstructure. The boundary region between Zone I and T is shifted to higher temperatures with increasing amount of impurities, since they limit the adatom mobility. With increasing temperature (Zone T), the impurities influence the competitive growth and the texture formation of the film. At low or medium levels, the impurities promote the growth of specific crystal faces, while others are blocked, which leads to a preferred orientation. In highly contaminated films the growth of all facets is blocked, as the impurities accumulate at the grain boundaries, hindering grain boundary mobility. Thus, competitive growth cannot occur and zone T does not evolve. The growth proceeds by repeated nucleation, leading to a globular structure of random orientation.

For low contamination levels, the boundary region between Zone T and Zone II is shifted to higher temperatures, whereas for high impurity levels Zone II does not appear.

At high substrate temperatures, the formation of a new Zone is observed. Zone III is controlled by impurity segregation, which restrains grain coarsening and the development of restructuration texture. The microstructure is formed of equiaxial (globular) grains and in the case of high impurity levels, Zone III will become nanocrystalline at low temperatures [24,26].

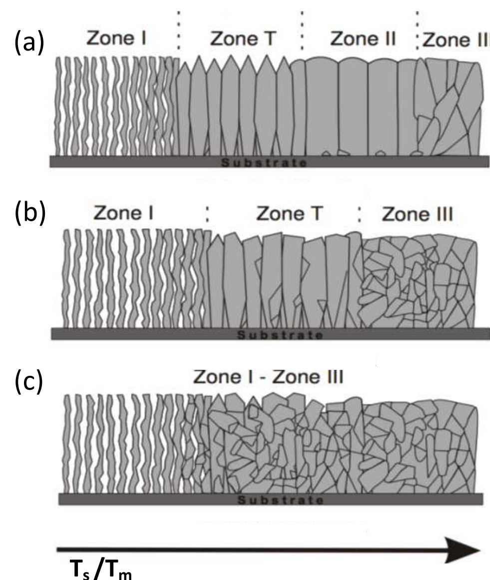

Fig. 2.7 Schematic of real SZMs of (a) low, (b) medium and (c) high impurity levels after [28].

2.3 Oxidation

2.3.1 Fundamentals of oxidation

The simplest oxidation reaction of a metal (M) with oxygen (O_2) is to form an oxide, which can be written as [29]:

$$xM + \frac{y}{2}O_2 \rightleftharpoons M_xO_y \quad (2.1)$$

There, x and y represent the stoichiometric factors.

Thermodynamically, the metal M will be oxidized if the oxygen partial pressure in the environment is greater than the dissociation pressure of the oxide. The dissociation pressure of an oxide p_{O_2} at a certain temperature T of exposure can be determined from the standard free energy of formation ΔG^0 as shown in Eq. 2.2 [30].

$$\Delta G^0 = RTlnp_{O_2} \quad (2.2)$$

Here, R is the general gas constant.

The standard free energies for the formation of oxides and the oxide dissociation pressures are plotted in Fig. 2.8 as a function of temperature in a so-called Richardson-Ellingham diagram. The lower the position of the curve of an oxide in the diagram, the more thermodynamically stable is the formed oxide and the lower is its dissociation partial pressure. The curve of $\Delta G°$ for most metal oxides has a positive slope with rising temperature, i.e the oxides become less stable with increasing temperature. Furthermore, the diagram is a useful tool for designing oxidation resistant alloys, since it directly compares the stability of various oxides. The metal of a more stable oxide tends to reduce the less stable oxide and be oxidized in the process. The curves of Al_2O_3 and Cr_2O_3 are more negative than most oxides (see Fig. 2.8). Accordingly, they are used as alloy elements in most high temperature materials, since they are most likely to prevent the oxidation of the base metal (such as Fe, Ni, Mo) by formation of stable oxides on the surface [30,31].

The Richardson-Ellingham diagram only gives information about the stability of the oxides, but not about the kinetics of the oxidation process. Often the reaction rate of the oxide formation is so slow, that although the formation of the oxide is thermodynamically possible, it takes very long to form [30].

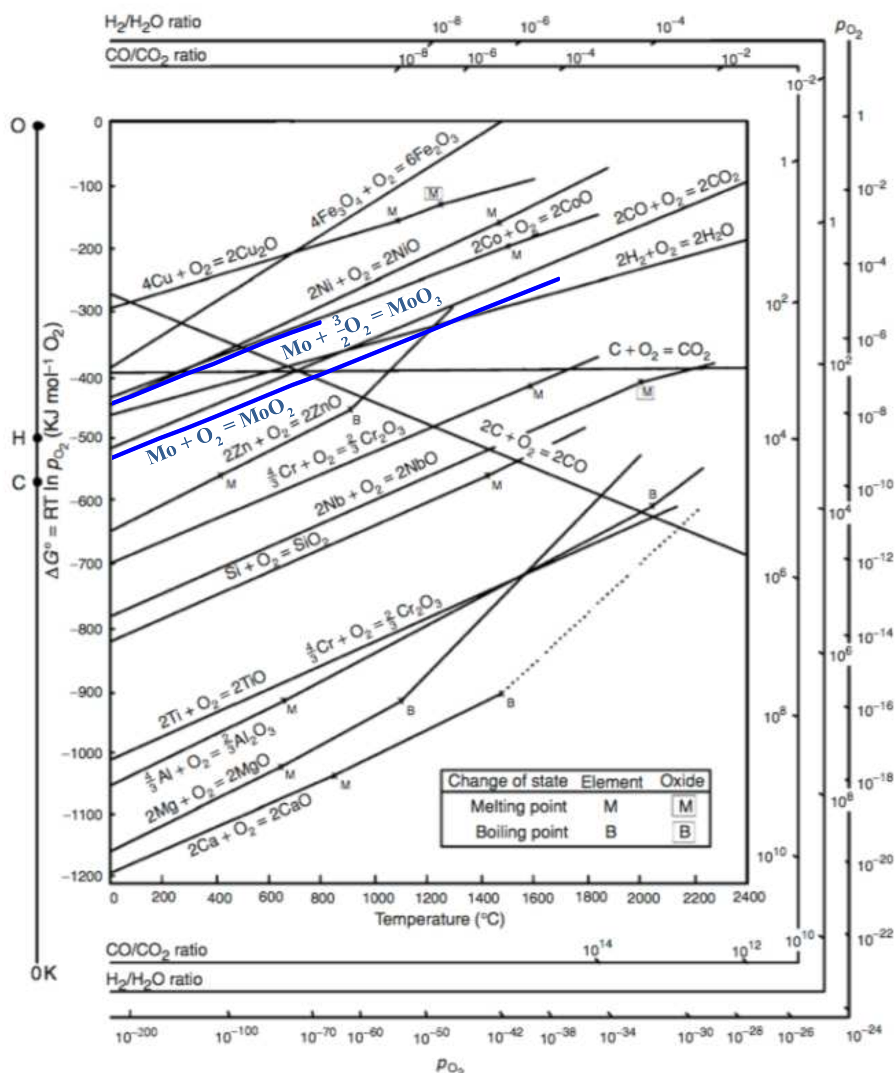

Fig. 2.8 Richardson-Ellingham diagram, showing the standard free energy of formation of various oxides [31], the ΔG° curves of molybdenum oxides (blue lines) were added from [32].

The processes that occur when a clean surface is exposed to oxygen are divided into two stages, the initial stage and the scale growth by solid state diffusion. The initial stage of the oxidation begins with adsorption and dissociation of oxygen on the metal surface, until a two-dimensional adsorption layer is formed. When the metal surface is saturated with adsorbed oxygen atoms, the oxygen dissolves into the metal. Then the formation of oxide nuclei takes place, which initially grow laterally to form a thin oxide film. The nucleation and growth of oxide nuclei is influenced by temperature and the oxygen partial pressure. After the formation of a thin and therefore transparent oxide layer, the growth of a thick oxide scale proceeds. Depending on whether the metal cations move faster through the oxide layer than the oxygen anions or vice versa, the film growth occurs either at the oxide/gas interface or at the oxide/metal interface, as shown in Fig 2.9 [31,33].

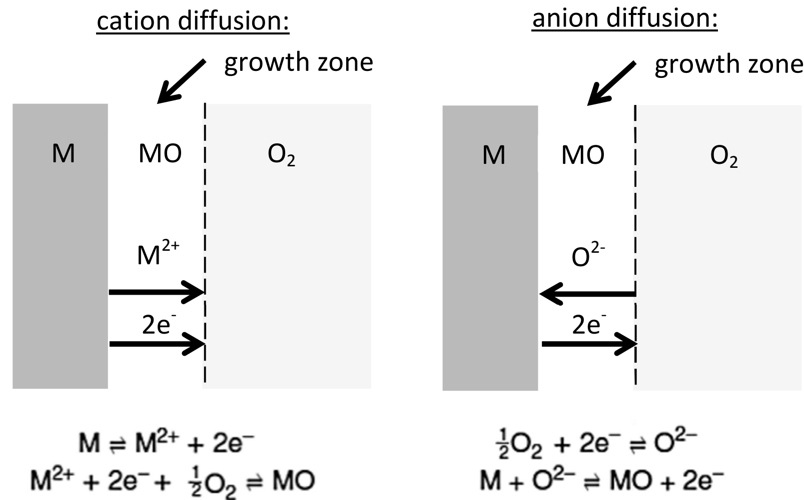

Fig. 2.9 Oxide layer growth by diffusion of cations and anions after [31].

Depending on material, temperature and test conditions, oxide film growth takes place according to different rate laws as shown in Fig. 2.10. In general, the oxidation rate laws of materials are determined gravimetrically by the weight change as a function of time. Most metals obey a logarithmic law, when heated at temperatures below 400°C. This behavior is associated with the formation of very thin oxide films (2-4 nm) [30,31].

At high temperatures linear, parabolic or "catastrophic" oxidation in form of volatile oxide formation can be observed. Metals and alloys which are applied in long-term high temperature applications usually follow the parabolic rate laws. The rate-determining step is diffusion of both ions and electrons through a compact oxide scale. Typical examples are Al, Cr and Si, which are known for their thick, dense and coherent oxide layers. Linear growth is characteristic for a very rapid oxidation, where the formed oxide is unable to prevent the access of oxygen to the metal surface. The two refractory metals Ta and Nb are oxidized approximately linearly at high temperatures [30,34,35].

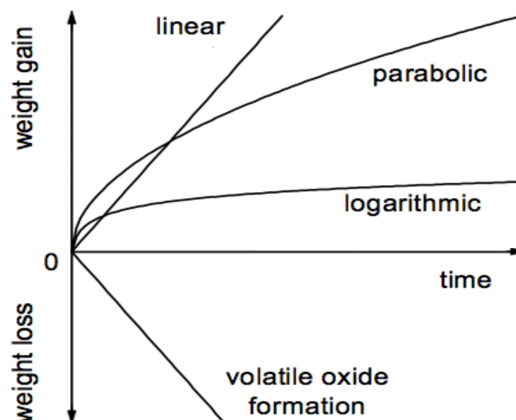

Fig. 2.10 The kinetics of oxidations after [34].

2.3.2 Oxidation behavior of Mo and Mo alloys

The oxidation behavior of Mo is strongly influenced by pressure and temperature as shown in Fig. 2.8. Mo oxidizes to form two binary oxides MoO_3 and MoO_2, which have been first systematically studied by Hägg and Magnéli [36]. They also reported the existence of intermediate molybdenum oxides with compositions between MoO_2-MoO_3, such as Mo_4O_{11}, Mo_8O_{23} and Mo_9O_{26}.
Both MoO_2 and MoO_3 form non-protective layers, which are responsible for the catastrophic oxidation behavior of Mo at high temperatures. Depending on temperature and oxygen partial pressure, following oxidation reactions can take place [37,38]:

$$Mo + O_2 \rightarrow MoO_2 \tag{2.3}$$

$$MoO_2 + \frac{1}{2}O_2 \rightarrow MoO_3 \tag{2.4}$$

$$Mo + \frac{3}{2}O_2 \rightarrow MoO_3 \tag{2.5}$$

At atmospheric pressure, a visible reaction between Mo and oxygen is observed above 200°C, with the tarnishing of the Mo surface. With increasing temperature, two oxide layers develop on the metal surface according to a parabolic rate law. An inner MoO_2 layer forms near the metal/oxide interface and an outer MoO_3 near the oxide surface. Above 500°C, the outer MoO_3 layer begins to volatilize and the formation and evaporation of the oxide takes place simultaneously. At 725°C, the rate-controlling process is the evaporation of MoO_3, which results in extremely rapid metal loss (see Fig. 2.10). The effect becomes catastrophic above the melting point of MoO_3 (795°C), as molten MoO_3 or a low-melting MoO_2-MoO_3 eutectic are formed [5,34].
In the past, various studies have been performed to enhance the poor oxidation resistance of Mo. It has been found that several alloying elements, including Si and Al, have a beneficial effect on the oxidation behavior of Mo. The improved oxidation resistance of those Mo alloys is based on the preferential oxidation of the solute elements and the formation of a continuous protective oxide scale. This process is often referred to as selective oxidation [39,40,31]. Habazaki et al. [41] investigated the oxidation behavior of sputter-deposited Al-Mo alloys. Due to the formation of a protective alumina scale, Al-Mo alloys exhibited a high oxidation resistance up to 800°C. In addition, they found that the presence of Si as a third alloying element further improved the oxidation resistance up to 900°C. Fig. 2.11 shows that the binary Al-34 Mo (at.%) alloy exhibits significant weight loss at 900°C, associated with the formation of volatile oxides. However, by adding small amounts of Si (6 at.%) no weight loss is observed at 900°C. Si is known to form a stable and highly protective SiO_2 scale and

supports the selective oxidation of Al. Due to the Al deficiency in Al-45Mo-21 alloy, weight loss is observed again.

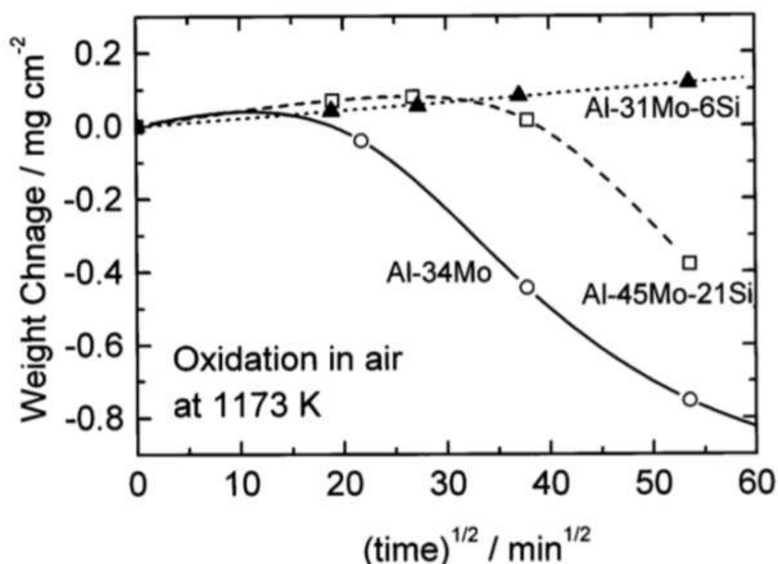

Fig. 2.11 The oxidation kinetics of the binary Al-Mo alloy and the ternary Al-Mo-Si at 900°C [41].

2.4 Wet etching

The wet etching process is an important step in the fabrication of TFT-LCDs. As part of photolithography, it is used to selectively remove sections of a deposited film in order to obtain a functional TFT array. In general, the photolithography sequence starts by transferring a pattern from a photomask to a photoresistant coating on the thin film. The patterned photoresist then acts as an etch mask for the deposited film. During the wet etching process, the underlying areas, which are not covered by the mask, are dissolved by a liquid etchant (see Fig. 2.12) [2,42].

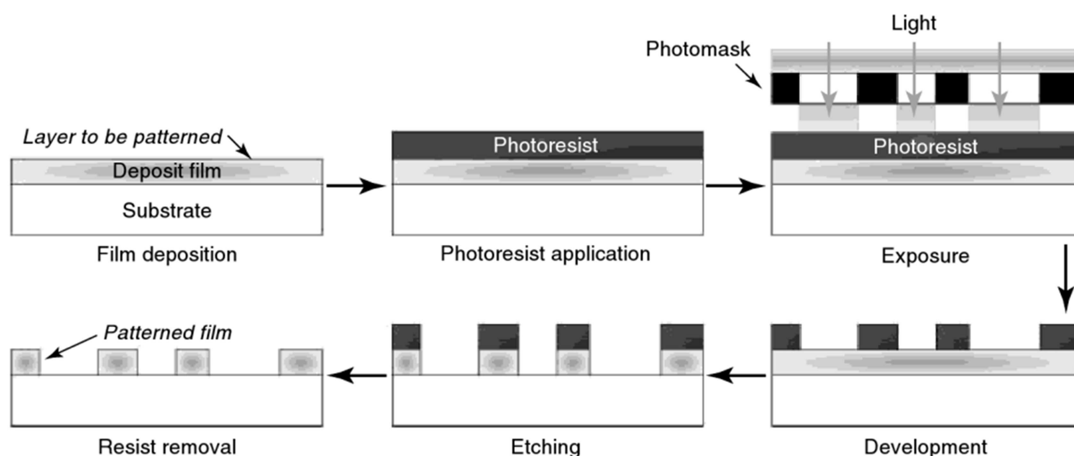

Fig. 2.12 Schematic of the photolithography process [42].

The basic wet etching mechanism includes diffusion of the liquid etchant to the surface, reaction at the surface and diffusion of the reaction products from the surface. Each of these steps can be rate-determining. If the wet etching is diffusion-limited, then the rate can be increased by rapid stirring of the etch solution. If the surface reaction is the rate limiting step, then the etching rate can be strongly influenced by temperature and composition of the etch solution [43,44].The principal electrochemical process, in which a metal (M) is dissolved by electron transfer, can be written as [45]:

$$M(s) \rightarrow M^{n+}(aq) + ne^- \quad (2.6)$$

Wet etching is the simplest method for dissolving metals in microelectronic fabrication and has found widespread use due to its low cost, high reliability and excellent selectivity [44,45]. The selectivity of the etchant is an important parameter in wet etching. The etchant should exhibit a high selectivity for the material, which is to be etched, and not attack the underlying layers [2].

2.4.1 Wet etching of Mo and Al

The most commonly used etchants for molybdenum and aluminum are based on mixtures of phosphoric acid (H_3PO_4), acetic acid (CH_3COOH) and nitric acid (HNO_3). Usually, the metals are first oxidized by the nitric acid, whereas the phosphoric acid dissolves the resulting oxides [45,46]. It has been reported by Kim et al. [47] that at low nitric acid concentrations the rate-determining step for etching of Mo is the formation of the metal oxide. However, with increasing HNO_3 concentrations, the oxidation of the metal is fast enough and the dissolution of the oxide is rate-determining. The corrosion potentials of Mo and Al, as well as the dissolution rate of Mo in phosphoric acid are plotted in Fig. 2.13 as a function of the nitric acid concentration. It shows that the corrosion and dissolution rate of Mo increase nearly linearly with increasing nitric acid concentration until a saturation value is reached at about 6 vol.%. In contrast, the corrosion potential of Al does not change significantly with increasing nitric acid concentration, thus the Al_2O_3 dissolution is the rate-determining step [47,48].

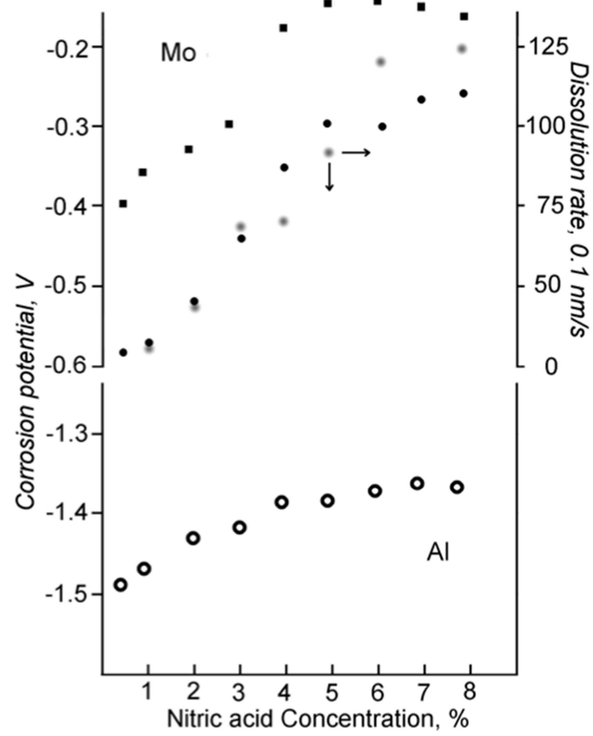

Fig. 2.13 Corrosion potentials of Mo and Al in phosphoric acid, ●○ at room temperature, ■ at 30°C and the dissolution rate of Mo (blurred circles) as a function of the nitric acid concentration [47].

Bibliography

[1] K. Oniawa, S. Takayama, Y. Shigesato, T. Takahashi, Metallization in a-Si:H TFT array fabrication, in Y. Kuo (ed.), "Thin Film Transistors Materials and Processes, Volume 1: Amorphous Silicon Thin Film Transistors", Kluwer Academic, Norwell, 2004, pp. 313-376.

[2] W. den Boer, "Active Matrix Liquid Crystal Displays", Newnes, Oxford, 2005, pp. 61-65.

[3] Y.W. Yen, Y.L. Kuo, J.Y. Chen, C. Lee, C.Y. Lee, Investigation of thermal stability of Mo thin-films as the buffer layer and various Cu metallization as interconnection materials for thin film transistor-liquid crystal display applications, Thin Solid Films 515 (2007) 7209-7216.

[4] J. Sarkar, "Sputtering Materials for VLSI and Thin Film Devices", William Andrew, Oxford, 2005, p. 44.

[5] K. Swars, "Gmelin Handbuch der anorganischen Chemie, Molybdän, Ergänzungsband Teil B1", Springer, Berlin, 1976, p. 29.

[6] L. Mele, F. Santagata, E. Iervolino, M. Mihailovic, T. Rossi, A.T. Tran, H. Schellevis, J.F. Creemer, P.M. Sarro, A molybdenum MEMS microhotplate for high-temperature operation, Sens. Actuators A 188 (2012) 173-180.

[7] A. List, C. Mitterer, G. Mori, J. Winkler, N. Reinfried, W. Knabl, Oxidation of sputtered thin films of molybdenum alloys at ambient conditions, in L.S Sigl, P. Rodhammer, H. Wildner (eds.), Proceedings of the 17th Plansee Seminar, Vol. 1, Plansee Group, Reutte, 2009, pp. RM 12/1-9.

[8] P.Y. Park, E. Akiyama, H. Habazaki, A. Kawashima, K. Asami, K. Hashimoto, The corrosion behavior of sputter-deposited Mo-Ti alloys in concentrated hydrochloric acid, Corros. Sci. 38 (1996) 1649-1667.

[9] K.R. Williams, R.S. Muller, Etch rates for micromachining processing, J. Microelectromech. Systems 5 (1996) 256-269.

[10] W.D Westwood, "Sputter deposition", AVS, New York, 2003.

[11] D.M. Mattox, "Handbook of Physical Vapor Deposition (PVD) Processing", 2nd ed., William Andrew, Oxford, 2010.

[12] M. Ohring, "Materials Science of Thin Films: Deposition and Structure", 2nd ed., Academic Press, San Diego, 2002.

[13] R.F. Bunshah, "Deposition Technologies for Films and Coatings", Noyes Publications, New Jersey, 1982.

[14] S.M. Rossnagel, Sputtering and sputter deposition, in K. Seshan (ed.) "Handbook of Thin-Film Deposition Processes and Techniques: Principles, Methods, Equipment, and Applications", 2nd ed., William Andrew, Norwich, 2002.

[15] D. Depla, S. Mahieu, J.E. Greene, Sputter deposition processes, in P.M. Martin (ed.), "Handbook of Deposition Technologies for Films and Coatings: Science", 3rd ed., William Andrew, Boston, 2010, pp. 253-294.

[16] R.A. Powell, S.M. Rossnagel, “PVD for Microelectronics: Sputter Deposition Applied to Semiconductor Manufacturing: Thin Films Vol. 26”, Academic Press, San Diego, 1999.

[17] H. Guo, J. Zhang, F. Li, Y. Liu, J. Yin, Y. Zhou, Surface strengthening of Ti3SiC2 through magnetron sputtering Cu and subsequent annealing, J. Eur. Ceram. Soc. 28 (2008) 2099-2107.

[18] J.E. Greene, Thin film nucleation, growth, and microstructural evolution: An atomic scale view, in P.M. Martin (ed.), “Handbook of Deposition Technologies for Films and Coatings”, 3rd ed., William Andrew, Boston, 2010, pp. 554-620.

[19] P.H. Mayrhofer, Materials Science Aspects of Nanocrystalline PVD Hard Coatings, PhD Thesis, Montanuniversität Leoben, 2001.

[20] R.D. Arnell, P.J. Kelly, Recent advances in magnetron sputtering, Surf. Coat. Technol. 112 (1999) 170-176.

[21] S.L. Rohde, Unbalanced magnetron sputtering, in M.H. Francombe, J.L. Vossen (eds.), “Physics of Thin Films, Vol. 18: Plasma Sources for Thin Film Deposition and Etching”, Academic Press, San Diego, 1994, pp. 235-285.

[22] P.M. Martin, “Introduction to Surface Engineering and Functionally Engineered Materials”, John Wiley & Sons, New Jersey, 2011.

[23] R.A. Haefer, “Oberflächen- und Dünnschicht-Technologie, Teil I, Beschichtungen von Oberflächen“, Springer, Heidelberg, 1987.

[24] P.B. Barna, M. Adamik, Growth mechanisms of polycrystalline thin films, in F.C. Matacotta, G. Ottaviani (eds.), “Science and Technology of Thin Films”, World Scientific, Singapore, 1995, pp. 1-28.

[25] P.B. Barna, M. Adamik, Fundamental structure forming phenomena of polycrystalline thin films and the structure zone models, Thin Solid Films, 317 (1998) 27-33.

[26] P.B. Barna, M. Adamik, Formation and characterisation of the structure of surface coatings, in Y. Pauleau, P.B. Barna (eds.), “Protective Coatings and Thin Films: Synthesis, Characterisation and Applications”, Kluwer Academic, Dordrecht, pp. 279-297.

[27] I. Petrov, P.B. Barna, L. Hultman, J.E. Greene, Microstructural evolution during film growth, J. Vac. Sci. Technol. A, 21 (2003) 117-128.

[28] P. Ghekiere, Structure Evolution of Biaxially Aligned Thin Films Deposited by Sputtering, PhD Thesis, Ghent University, 2007.

[29] S. Leistikow, Thermodynamik und Kinetik der Oxidbildung, in A. Rahmel (ed.), “Aufbau von Oxidschichten auf Hochtemperaturwerkstoffen und ihre technische Bedeutung”, Deutsche Gesellschaft für Metallkunde, Frankfurt, 1982, pp. 33-56.

[30] A.S. Khanna, “Introduction to High Temperature Oxidation and Corrosion”, ASM International, Materials Park, 2002.

[31] N. Birks, G.H. Meier, F.S. Pettit, “Introduction to the High Temperature Oxidation of Metals”, Cambridge University Press, Cambridge, 2006.

[32] University of Cambridge, The interactive Ellingham diagram, http://www.doitpoms.ac.uk/tlplib/ellingham_diagrams/interactive.php, February 2014.

[33] M. Schütze, Fundamentals of high temperature corrosion, in M. Schütze (ed.), “Corrosion and Environmental Degradation Vol. I”, Wiley-VCH, Weinheim, 2000, pp. 67-130.

[34] K.R. Trethewey, J. Chamberlain, “Corrosion for Students of Science and Engineering”, Longman, Harlow, 1988. pp. 335-344

[35] R. Bürgel, “Handbuch Hochtemperatur-Werkstofftechnik”, 3rd ed., Vieweg, Wiesbaden, 2006.

[36] G. Hägg, A. Magnéli, X-ray studies on molybdenum and tungsten oxides, Arkiv Kemi Mineral. Geol. 19 (1945) 1-14.

[37] J.H. Perepezko, R. Sakidja, K.S. Kumar, Mo-Si-B alloys for ultrahigh temperature applications, in O.W. Soboyejo, T.S. Srivatsan (eds.), “Advanced Structural Materials: Properties, Design Optimization, and Applications”, CRC Press, Boca Raton, 2006, pp. 437-474.

[38] V.M. Balsaraf, “Applied Chemistry- II”, I.K. International, New Dehli, 2009.

[39] M. Meyer, M. Kramer, M. Akinc, Boron-doped molybdenum silicides, Advanced Materials 261 (1996) 85-88.

[40] S. Paswan, R. Mitra, S.K. Roy, Isothermal oxidation behaviour of Mo–Si–B and Mo–Si–B–Al alloys in the temperature range of 400–800°C, Mater. Sci. Engin., A 424 (2006) 251-265.

[41] H. Habazaki, K. Hon-yashiki, K. Ito, H. Mitsui, A. Kawashima, K. Asami, K. Hashimoto, S. Mrowec, Sulfidation- and oxidation-resistant alloys prepared by sputter deposition, Mater. Sci. Engin., A 267 (1999) 267-276.

[42] F. Li, A. Nathan, Y. Wu, B. S. Ong, “Organic Thin Film Transistor Integration: A Hybrid Approach”, Wiley-VCH, Weinheim, 2011, p. 65

[43] M.A. Huff, Medical application of micro-electro-mechanical systems (MEMS) technology, in Y. Rosen, N. Elman (eds.), “Biomaterials Science: An Integrated Clinical and Engineering Approach”, CRC Press, Boca Raton, 2012, pp. 29-84.

[44] N.P. Mahalik, “MEMS”, Tata McGraw-Hill, New Dehli, 2007, pp. 58-63.

[45] M. Liu, Z. Ji, L. Shang, Top-down fabrication of nanostructures, in L. Chi (ed.), “Nanotechnology: Volume 8: Nanostructured Surfaces”, Wiley-VCH, Weinheim, 2010, pp. 1-43.

[46] D.W. Burns, MEMS wet-etch processes and procedures, in R. Ghodssi, P. Lin (eds.), “MEMS Materials and Processes Handbook”, Springer, New York, 2011, pp. 457-665.

[47] I.S. Kim, S. Chon, K.S. Kim, C. Jeon, Dissolution of Mo/Al bilayers in phosphoric acid, B. Kor. Chem, Soc. 24 (2003) 1613-1617.

[48] S. Franssila, “Introduction to Microfabrication”, John Wiley & Sons, Chichester, 2004, pp. 119-121.

3 Manuscript

Oxidation and wet etching behavior of sputtered Mo-Ti-Al films

T. Jörg[1], A.M. Hofer[1], J. Winkler[2], H. Köstenbauer[2], C. Mitterer[1]

1 Department of Physical Metallurgy and Materials Testing, Montanuniversität Leoben, Franz-Josef-Straße 18, 8700 Leoben, Austria

2 PLANSEE SE, Metallwerk-Plansee-Straße 71, 6600 Reutte, Austria

Abstract

Exposure of molybdenum thin films above 300°C in ambient atmosphere result in surface oxidation, leading to the formation of colored oxide films deteriorating their application in thin film transistor liquid crystal displays. In this study, the influence of alloying titanium and aluminum on microstructure, electrical properties, oxidation and wet etching behavior of thin films was investigated. Mo-Ti-Al films with 8 at.% Ti and different Al contents (8-24 at.%) were deposited by d.c magnetron sputtering and annealed in ambient air at 330°C for 1 h. The oxidation resistance of Mo-Ti-Al films was enhanced with increasing Al content. A minimum alloy content of 16 at.% Al was necessary to form a thin protective Al_2O_3 surface layer and prevent the formation of colored molybdenum oxides. The wet etching ability of the Mo-Ti-Al films in phosphoric, acetic, nitric acid decreased with increasing Al content, but was still acceptable for thin film transistor liquid crystal displays applications.

Keywords: molybdenum, alloying, oxidation, sputtering, wet etching

1. Introduction

Sputtered molybdenum (Mo) thin films are used in thin film transistor liquid crystal displays (TFT-LCD) as conducting materials. Their low electrical resistance and easy chemical patterning make them an excellent material for source/drain electrodes and data bus-lines. Furthermore, Mo thin films are used as bottom and capping layers in the gate metallization of TFTs, due to their good adhesion on glass and low contact resistance to silicon and indium tin oxide [1]. They also serve as diffusion barrier, since Mo exhibits a high melting point and very low diffusion coefficients [2,3].

Since annealing treatments are used in TFT-LCD processing [4], these films have to withstand thermal exposure without deterioration of their properties. However, Mo is known to exhibit poor oxidation resistance in air and is prone to oxidation above 300° C [5,6]. Alloying of Mo thin films has been suggested to improve their oxidation resistance [7]. For example, Park et al. have reported that Ti is corrosion resistant in oxidizing atmospheres and that alloying of Ti to Mo leads to the formation of a passivation layer [8]. However, Ti cannot be dissolved in phosphoric, acetic, nitric acid solutions (PAN), which is a key process step in the production of TFT materials [9].

The aim of the present work is to study the oxidation resistance and wet etching ability of ternary Mo-Ti-Al alloys with varying Al contents, where Al is known for its superior oxidation resistance and good wet etching behavior in PAN [9]. Film microstructure and properties are investigated in order to determine the influence of the alloying elements.

2. Experimental details

The films were deposited on silicon (100) and glass substrates (Corning EAGLE2000TM AMLCD), using a laboratory-scale unbalanced d.c. magnetron sputter system. The silicon substrates and glass substrates were ultrasonically cleaned in ethanol or a commercial detergent from Borer Chemie AG, respectively. The films were deposited using one powder-metallurgically prepared $Mo_{90}Ti_{10}$ and one Al target (ø 50.8 × 6.35 mm^2), which were mounted on two unbalanced AJA magnetrons. The substrates were fixed on a rotatable sample holder positioned about 55 mm above the magnetrons. The vacuum chamber was evacuated to a base pressure of $\leq 2 \times 10^{-3}$ Pa. Prior to deposition, the substrates were plasma etched with using a pulsed d.c. discharge at -500 V and 250 kHz for 2 min. Different Al contents within the films were obtained by varying the d.c. current on the Al target between 0 and 0.15 A, whereas the $Mo_{90}Ti_{10}$ target was operated at a constant value (0.35 A). An Ar flow of 15 sccm resulted in a working pressure of 2.0×10^{-2} Pa.

The fracture cross-sections of the films on the Si substrates were investigated with a scanning electron microscope (SEM, Zeiss Evo-50) to evaluate the deposition rate. Furthermore, energy-dispersive X-ray spectroscopy (EDX, Oxford Instruments INCA), attached to the SEM was used to determine the chemical composition of the films on the Si substrates. To obtain a film thickness of approximately 300 nm for all films, the deposition times were varied for each deposition condition, being between 6 and 9 min. All further investigations were conducted on the glass substrate films.

A standard four-point probe technique was used to measure the electrical resistivity of the films. The characterization of the crystal structure was done by X-ray diffraction (XRD)

measurements using a Bruker AXS D8 Advance diffractometer with CuKα radiation (λ = 1.5418 Å) and Bragg-Brentano geometry.

The wet etching rate of the as-deposited films was determined by the weight difference of the substrate before and after dipping in the etchant. The etching solution (PAN) was composed of 66% phosphoric acid, 10% acetic acid and 5% nitric acid by volume. All wet etchings were performed at a stirring rate of 300 rpm at 40°C.

To evaluate the oxidation behavior of the films, as-deposited samples were annealed in a chamber furnace in air at 330°C for 1 h. Reflectance UV–Vis spectra of the films were measured before and after annealing using a Perkin Elmer Lambda 950 photo-spectrometer. The Raman spectra were measured using a Jobin Yvon LabRam confocal Raman spectrometer employing a Nd:YAG laser (λ = 532 nm, 10 mW). The oxidation states of the films after annealing were studied by X-ray photoelectron spectroscopy (XPS) using an Omicron Multiprobe system with a monochromized Al K_α beam (1486.6 eV) and a resolution < 0.5 eV. In order to remove the volatile surface contaminants, the samples were heated for 20 min at 300°C before XPS measurements.

3. Results and discussion

3.1. As-deposited films

3.1.1. Chemical composition and microstructure

The chemical compositions of the Mo-Ti-Al films deposited at different Al currents are shown in Table 1. As the current on the Al target increases from 0 to 0.15 A, the ratio of Ti:Al almost linearly increases from 1:1 via 1:2 to 1:3 with a corresponding decrease of the Mo content. In the subsequent text, films will be denominated by the formula given in the column "sample" in Table 1.

Table 1

Chemical composition of the MoTiAl films as analyzed by EDX.

Sample	Current (Al target)	Chemical composition			Film thickness
		Mo	Ti	Al	
	[A]		[at. %]		[nm]
$MoTi_8$	0	91.9	8.1	-	253
$MoTi_8Al_8$	0.05	84.1	8.3	7.5	264
$MoTi_8Al_{16}$	0.1	76.3	8.2	15.5	235
$MoTi_6Al_{24}$	0.15	69.6	6.5	23.9	253

Fig. 1 illustrates the XRD diffractograms of the Mo-Ti-Al alloy films in the as-deposted state. All films are polycrystalline and consist of a body-centered cubic (bcc) phase. The positions of the diffraction peaks of Mo (2Θ = 40.50°, 58.61°, 73.67°, 87.62°), indicated in Fig. 1, correspond well to those of the peaks observed for the Mo-Ti-Al films [10]. Accordingly, all thin films consist of a bcc single-phase Mo-based solid solution. The diffraction peaks of the $MoTi_8$ film shift to lower diffraction angles, compared to the unalloyed Mo film, indicating an obvious increase of interplanar lattice distance in the film. This is attributed to the replacement of Mo atoms by larger Ti atoms. With increasing Al content, the peaks of the Mo-Ti-Al films slightly shift to higher diffraction angles compared to the Mo reference. This is a result of a lower interplanar lattice distance and thus a decreasing lattice parameter, which evidences that the film lattice contracts with the substitution of Mo by smaller Al atoms. All films show a preferred (110) orientation. However, the intensity of the (110) peak decreases with increasing Al content, while (200) peaks emerge.

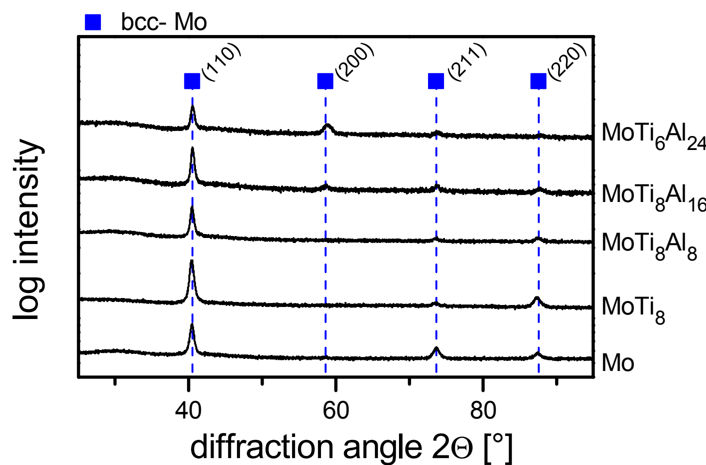

Fig. 1. XRD diffractograms of Mo-Ti-Al films with different Al contents compared to an unalloyed Mo film.

3.1.2. Wet etching behavior

The wet etching rate of Mo-Ti-Al alloys as a function of the Al content is plotted in Fig. 2. The dissolution rate of the Mo-Ti-Al films in PAN gradually decreases with increasing Al content. This is in good agreement to Kim et al., who reported that Mo exhibits a higher wet etching rate than Al in phosphoric nitric acid and that the contact of the less noble Al decreases the dissolution rate of the nobler Mo [11].

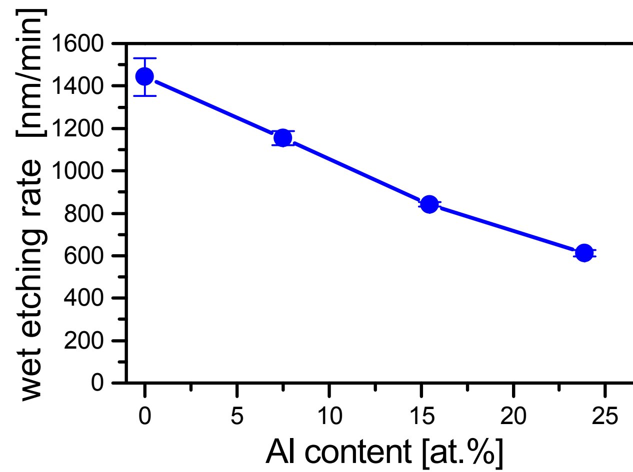

Fig. 2. Wet etching rate of Mo-Ti-Al films as a function of the Al content.

3.2. Annealed films

3.2.1. Electrical resistivity

The influence of the Al content on the electrical resistivity of the Mo-Ti-Al films is shown in Fig. 3. A pure Mo film (300 nm thick), as reported in our earlier work [12], has a resistivity of about 10 µΩcm. Alloying 8 at.% Al to the $MoTi_8$ solid solution causes a sharp rise of electrical resistivity to approximately 100 µΩcm. However, further Al additions results in a linear increase of the resistivity. This behavior can be explained by the different atom size of the alloying elements, which lead to an increase of electron scattering. Furthermore, alloying elements introduce local charge differences, due to their different valence electrons, which results in a higher scattering probability [13].

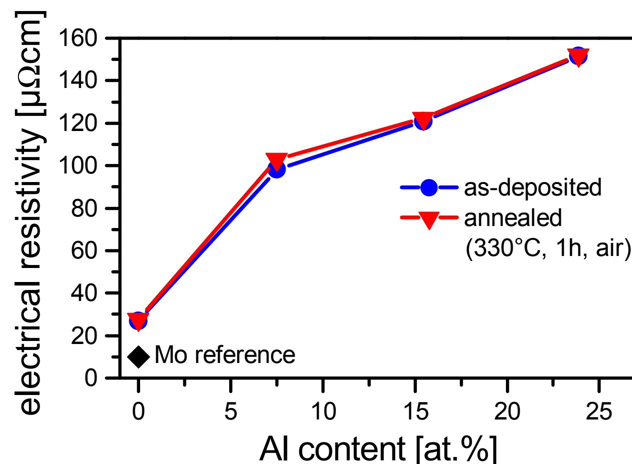

Fig. 3. Electrical resistivity of the Mo-Ti-Al films as a function of the Al content in the as-deposited and annealed state. The electrical resistivity of a 300 nm Mo film reported in our earlier work [12] is given as a reference.

No significant difference between the electrical resistivity before and after annealing is observed. This may be attributed to the fact that the oxide films formed during annealing are too thin to affect the measurement.

3.2.2. Optical properties

Annealing of the as-deposited samples in air at 330°C results in the formation of colored oxide films (see Fig. 4). However, the Mo-Ti-Al films with 16 at.% Al and 24 at.% Al remain colorless after the heat treatment, indicating the formation of a very thin transparent oxide film.

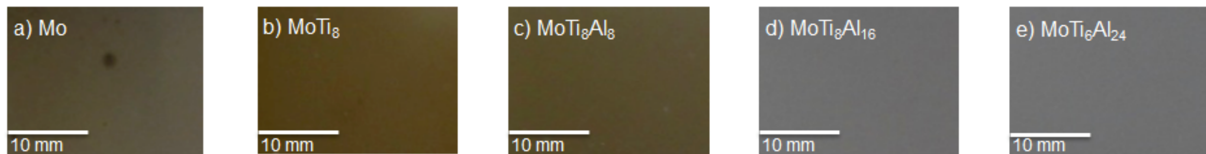

Fig. 4. Photographs of the investigated films after annealing at 330°C for 1 h in air.

The reflectance spectra of the $MoTi_8Al_8$ and $MoTi_8Al_{16}$ films in the as-deposited and annealed state are presented in Fig. 5. Both films show in the as-deposited state an average reflectance of above 50 %, confirming the metallic appearance. Moreover, it can be seen that the Al fraction in the films has a strong influence on the optical properties of the annealed samples. The reflectance of the Mo film containing 8 at.% Al decreases significantly after annealing and shows an absorption edge below 400 nm. The strong absorption in the violet region of the spectrum is responsible for the yellowish color of the film (see Fig. 4c) and indicates the formation of an oxide layer.

However, by increasing the Al content to 16 at.%, the decrease in reflectivity after annealing is reduced and the formation of the absorption edge is prevented. As a result, the optical appearance remains metallic (see Fig. 4d).

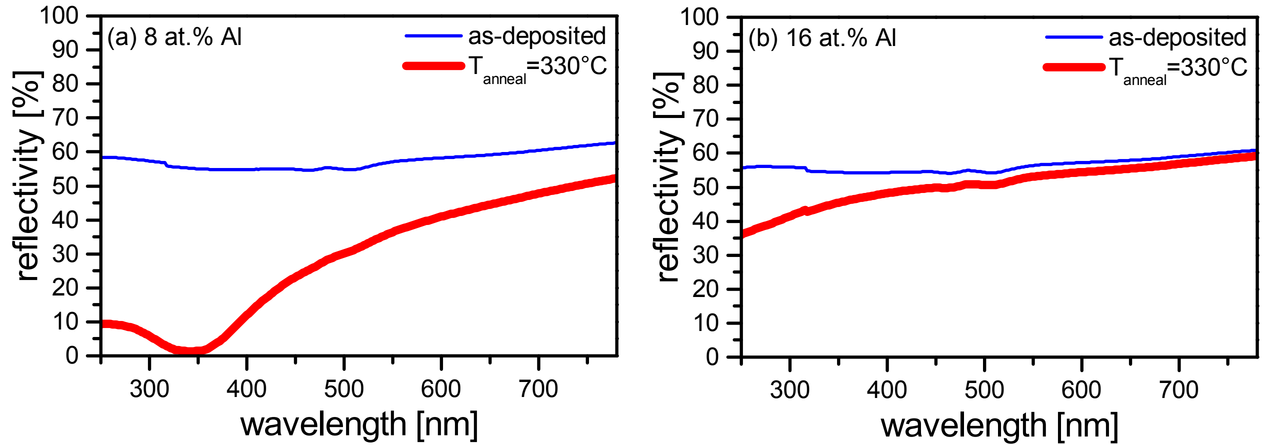

Fig. 5. Optical reflectance spectra before and after annealing of (a) $MoTi_8Al_8$ and (b) $MoTi_8Al_{16}$.

3.2.3. Oxidation states

The oxide films formed during annealing are too thin to be detected by XRD and in SEM cross-sections. To obtain more information about the surface oxides, which are responsible for the thermal coloration of the films, Raman spectroscopy was performed. Molybdenum oxides are well suited for characterization by Raman scattering [14]. In contrast, annealing of bulk Al below 350°C leads to the formation of an amorphous Al_2O_3 film [15], which can not be detected by Raman spectroscopy [16,17].

Fig. 6 illustrates the Raman spectra of the annealed samples, which are in good agreement with the results of visual inspection and UV-Vis spectroscopy. The Raman spectrum of the reference Mo film corresponds to the characteristic peaks of the polycrystalline MoO_3 bands (995 cm^{-1}, 818 cm^{-1} and 665 cm^{-1}). Therefore, it can be concluded that the annealing treatment causes surface oxidation of the unalloyed Mo film and leads to the formation of MoO_3. The Raman bands of the $MoTi_8$ and $MoTi_8Al_8$ film are nearly identical. Both spectra exhibit broadening of the peaks, suggesting the presence of mixed oxides [18]. In contrast, no Raman peaks are observable for the Mo-Ti-Al films with 16 at.% Al and 24 at.% Al, indicating the absence of the Raman-active MoO_3 and TiO_2. Thus, it can be concluded that an increased Al content prevents formation of MoO_3 and results in growth of a protective Al_2O_3 film.

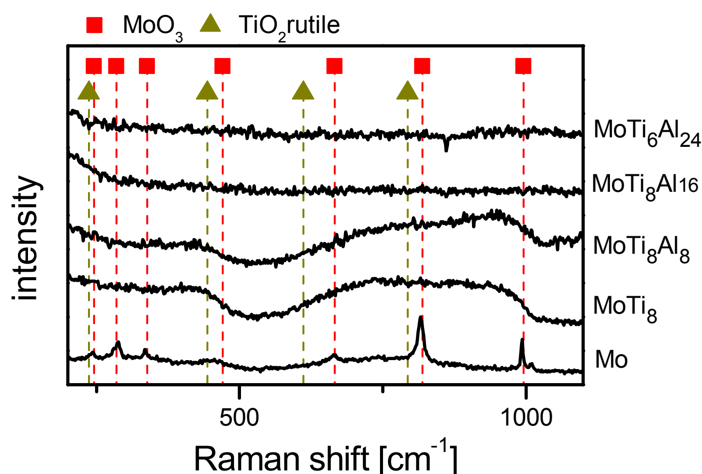

Fig. 6. Raman spectra of the Mo-Ti-Al films compared to a Mo reference after annealing at 330°C for 1h in air.

In order to study the influence of Al on the oxidation states of Mo and to verify the presence of the assumed Al_2O_3 film, XPS analyses were conducted. As a result of spin-orbit (j-j) coupling, the Mo3d spectrum consists of the characteristic Mo3$d_{5/2}$-Mo3$d_{3/2}$ doublet [19]. Fig. 7 shows the Mo3d XPS spectra of the Mo-Ti-Al films with different Al contents. Again, the spectra of the $MoTi_8$ and Mo-Ti-Al film with 8 at.% Al exhibit substantial similarity. Curve fitting of the Mo3$d_{5/2}$ peak indicates two spectral lines at 231.8 and 232.7 eV, which are assigned to Mo^{5+} and Mo^{6+} states. These peak positions agree well with earlier reports [20]. Clearly, the intensity of the Mo^{6+} oxidation state exceeds the one of the Mo^{5+} oxidation state and is the major contribution to the Mo3$d_{5/2}$ signal of the $MoTi_8$ and $MoTi_8Al_8$ films. Thus, it can be concluded that annealing the low-alloyed films in air is enhancing the Mo^{6+} state and therefore the formation of MoO_3.

However, the XPS spectra of the Mo-Ti-Al films alter with increasing Al content. For the Mo-Ti-Al film with 16 at.% Al several oxidation states can be identified, with binding energies of the Mo3$d_{5/2}$ corresponding to metallic Mo^0 (227.9 eV), Mo^{4+} (229.1 eV), Mo^{5+} (232.0 eV) and Mo^{6+} (233.1 eV). Similar finding have also been reported by Kim et al [21].As the Al content is further increased, the same oxidation states and one additional species of Mo is observed, with a binding energy of 228.3 eV. Since the binding energy of this oxidation state is between Mo^{4+} and the metallic Mo^0, it is referred to as $Mo^{\delta+}$. Choi et al. assigned this Mo species to Mo^{3+}, Xiang et al. to Mo^{2+} [19,22]. Increasing the Al content decreases the intensity of the Mo^{6+} peaks and favors reduced oxidation states of Mo. Accordingly, the intensity of the metallic Mo^0 peak is the highest observed in the $MoTi_6Al_{24}$ film (see Fig. 7).

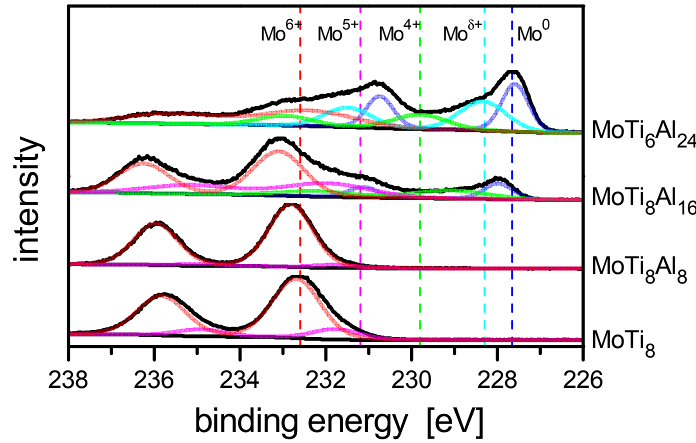

Fig. 7. Mo3d XPS spectra of Mo-Ti-Al films with different Al contents.

The results of peak area analysis of the Ti2p and Al2p bands are summarized in Table 2. It shows that an increasing Al content leads to enhanced formation of Al_2O_3. As a consequence, it can be presumed that the formation of Al_2O_3 is responsible for the reduced oxidation states of Mo. Therefore, the oxidation behavior of Mo-Ti-Al films is primarily controlled by the Al content in the films. The same effect was reported by Kai et al. for an investigation of the oxidation of a Zr-Cu-Al-Ni amorphous alloy in air at 300–425°C [23].

Table 2

Quantitative peak area analysis of the Ti2p and Al2p XPS bands

Sample	Quant. [%]			
	Ti (453.9 eV)	TiO_2 (458.9 eV)	Al (72.3 eV)	Al_2O_3 (74 eV)
$MoTi_8$	-	2.51	-	-
$MoTi_8Al_8$	-	2.61	-	3.58
$MoTi_8Al_{16}$	-	2.59	0.18	7.18
$MoTi_6Al_{24}$	0.15	2.45	1.59	11.29

4. Conclusions

The influence of different Al contents on the microstructure, wet etching behavior and oxidation resistance of Mo-Ti-Al films deposited by d.c magnetron sputtering was investigated. All films show a single-phase body-centered cubic structure based on the Mo phase. An increasing Al content results in a decline of the wet etching behavior of the Mo alloy films in a 66 vol.% phosphoric acid, 10 vol.% acetic acid and 5 vol.% nitric acid (PAN), but is still in an acceptable range for thin film transistor liquid crystal display applications.

The formation of MoO_3 during the annealing at 330°C for 1 h is responsible for the thermal coloration of the unalloyed Mo and the low-alloyed Mo-Ti-Al (i.e., 8 at.% Ti without Al and with 8 at.% Al, respectively) films. The further increasing Al content promotes the formation of an amorphous Al_2O_3 layer, which reduces the oxidation states of Mo. Therefore, the oxidation behavior of Mo-Ti-Al films is primarily controlled by the Al content, where a minimum alloying element content of 8 at.% Ti and 16 at.% Al was found to be necessary to enhance the oxidation resistance at still acceptable wet etching rates.

Acknowledgement

This work was done within the Competence Headquarters Project E^2-Sputtertech, with financial support from the Österreichische Forschungsförderungsgesellschaft. The authors are grateful to Alexander Fian (Joanneum Research, Weiz, Austria) for XPS measurements and to Dr. Ronald Bakker (Montanuniversität Leoben) for the assistance with Raman spectroscopy.

References

[1] K. Oniawa, S. Takayama, Y. Shigesato, T. Takahashi, Metallization in a-Si:H TFT array fabrication, in Y. Kuo (ed.), "Thin Film Transistors Materials and Processes, Volume 1: Amorphous Silicon Thin Film Transistors", Kluwer Academic, Norwell, 2004, pp. 313-376.

[2] W. den Boer, "Active Matrix Liquid Crystal Displays", Newnes, Oxford, 2005, pp. 61-65.

[3] Y.W. Yen, Y.L. Kuo, J.Y. Chen, C. Lee, C.Y. Lee, Investigation of thermal stability of Mo thin-films as the buffer layer and various Cu metallization as interconnection materials for thin film transistor-liquid crystal display applications, Thin Solid Films 515 (2007) 7209-7216.

[4] J. Sarkar, "Sputtering Materials for VLSI and Thin Film Devices", William Andrew, Oxford, 2005, p. 44.

[5] K. Swars, "Gmelin Handbuch der anorganischen Chemie, Molybdän, Ergänzungsband Teil B1", Springer, Berlin, 1976, p. 29.

[6] L. Mele, F. Santagata, E. Iervolino, M. Mihailovic, T. Rossi, A.T. Tran, H. Schellevis, J.F. Creemer, P.M. Sarro, A molybdenum MEMS microhotplate for high-temperature operation, Sens. Actuators A 188 (2012) 173-180.

[7] A. List, C. Mitterer, G. Mori, J. Winkler, N. Reinfried, W. Knabl, Oxidation of sputtered thin films of molybdenum alloys at ambient conditions, in L.S Sigl, P. Rodhammer, H. Wildner (eds.), Proceedings of the 17th Plansee Seminar, Vol. 1, Plansee Group, Reutte, 2009, pp. RM 12/1-9.

[8] P.Y. Park, E. Akiyama, H. Habazaki, A. Kawashima, K. Asami, K. Hashimoto, The corrosion behavior of sputter-deposited Mo-Ti alloys in concentrated hydrochloric acid, Corros. Sci. 38 (1996) 1649-1667.

[9] K.R. Williams, R.S. Muller, Etch rates for micromachining processing, J. Microelectromech. Systems 5 (1996) 256-269.

[10] Powder diffraction file (Card: 00-004-0809 for bcc-Mo). International Center for Powder Diffraction Data, ICDD, 2007. PDF-2.

[11] I.S. Kim, S. Chon, K.S. Kim, C. Jeon, Dissolution of Mo/Al bilayers in phosphoric acid, B. Kor. Chem, Soc. 24 (2003) 1613-1617.

[12] A.M. Hofer, J. Schlacher, J. Keckes, J. Winkler, C. Mitterer, Sputtered molybdenum films: Structure and property evolution with film thickness, Vacuum 99 (2014) 149-152.

[13] R.E. Hummel, "Electronic Properties of Materials", Springer, New York, 2005, pp. 88-89.

[14] T. He, J. Yao, Photochromism of molybdenum oxide, J. Photoch. Photobio. C 4 (2003) 125-143.

[15] N. Birks, G. H. Meier, F.S. Pettit, "Introduction to the High Temperature Oxidation of Metals", Cambridge University Press, Cambridge, 2006, p. 82.

[16] J. Xu, H. Ju, L. Yu, Microstructure, oxidation resistance, mechanical and tribological properties of Mo-Al-N films by reactive magnetron sputtering, Vacuum 103 (2014) 21-27.

[17] G. Xiong, J. W. Elam, H. Feng, C. Y. Han, H. Wang, L.E. Iton, L.A. Curtiss, M.J. Pellin, M. Kung, H. Kung, P.C. Stair, Effect of atomic layer deposition coatings on the surface structure of anodic aluminum oxide membranes, J. Phys. Chem. B 109 (2005) 14059-14063.

[18] J. Miciukiewicz, T. Mang, H. Knözinger, Raman spectroscopy characterization of molybdena supported on titania-zirconia mixed oxide, Appl. Catal. A 122 (1995) 151-159.

[19] J.G. Choi, L.T. Thompson, XPS study of as-prepared and reduced molybdenum oxides, Appl. Surf. Sci. 93 (1996) 143-149.

[20] S. Marika, E. Morán, C. Labrugére, O. Toulemonde, M.A. Alario-Franco, $Mo_xCu_{1-x}Sr_2YCu_2O_y$ (0.3≤x≤1) revisited: Superconductivity, magnetism and the molybdenum oxidation state, J. Solid State Chem. 191 (2012) 40-45.

[21] D. Kim, S.V. Kagwade, C.R. Clayton, Identification of Mo(V) commonly observed in passive films formed on stainless steels, Surf. Interf. Anal. 26 (1998) 155-159.

[22] M. Xiang, D. Li, H. Qi, W. Li, B. Zhong, Y. Sun, Mixed alcohols synthesis from carbon monoxide hydrogenation over potassium promoted β-Mo_2C catalysts, Fuel 86 (2007) 1298–1303.

[23] W. Kai, H.H. Hsieh, T.G. Nieh, Y. Kawamura, Oxidation behavior of a Zr–Cu–Al–Ni amorphous alloy in air at 300–425°C, Intermetallics 10 (2002) 1265-1270.

Appendix

This appendix contains additional data of ternary Mo-X-Y (X=Ti or Mg, Y=Al or Ni) films, which were also investigated within the scope of the thesis. All ternary Mo films were synthesized and characterized as described in section 2. Table 1 presents the chemical composition, film thickness and electrical resistivity before and after annealing of all films analyzed. It should be noted that the formula given in the column "Sample" represents the alloying content of the film in at.%. As shown in Table 1, two ternary Mo-Ti-Al systems, one with lower and the other with higher Ti content, were examined. The amount of Al was systematically increased within these systems to determine the effect of the alloying concentration on the properties of the films. In addition, a ternary Mo-Mg-Al film and two Mo-Ti-Ni reference films were also studied as part of this thesis.

Table 1

Chemical composition, film thickness and electrical resistivity of all films investigated.

Sample (alloying content [at.-%])	Film thickness [nm]	Electrical resistivity [µΩcm]	
		as-deposited	annealed
$MoTi_8$	253	26.9	27.8
$MoTi_8Al_8$	264	98.2	103.0
$MoTi_8Al_{16}$	235	120.9	122.4
$MoTi_6Al_{24}$	253	151.5	152.2
$MoTi_{17}$	231	40.0	41.3
$MoTi_{16}Al_9$	260	94.4	96.0
$MoTi_{15}Al_{16}$	270	125.4	126.4
$MoTi_{14}Al_{24}$	264	152.1	154.5
$MoTi_{13}Ni_{14}$	235	88.3	87.6
$MoTi_{12}Ni_{20}$	260	100.7	100.5
$MoMg_9Al_{23}$	275	203.6	204.9

As reported in section 3.2.1, the electrical resistivity increases with increasing alloy concentration. The same behavior is observed for all ternary Mo films (see Table 1). The resistivity of the Mo-Ti-Ni films is slightly lower than that of the Mo-Ti-Al films, but they are still in the same order of magnitude. The Mo-Mg-Al film exhibits the highest resistivity of all films investigated.

The results of XRD analysis of the additional ternary Mo alloy films in the as-deposited state are summarized in Fig. 1. The XRD diffractograms show, that all alloying elements form solid solutions with Mo. This is in accordance with the finding in section 3.1.1.

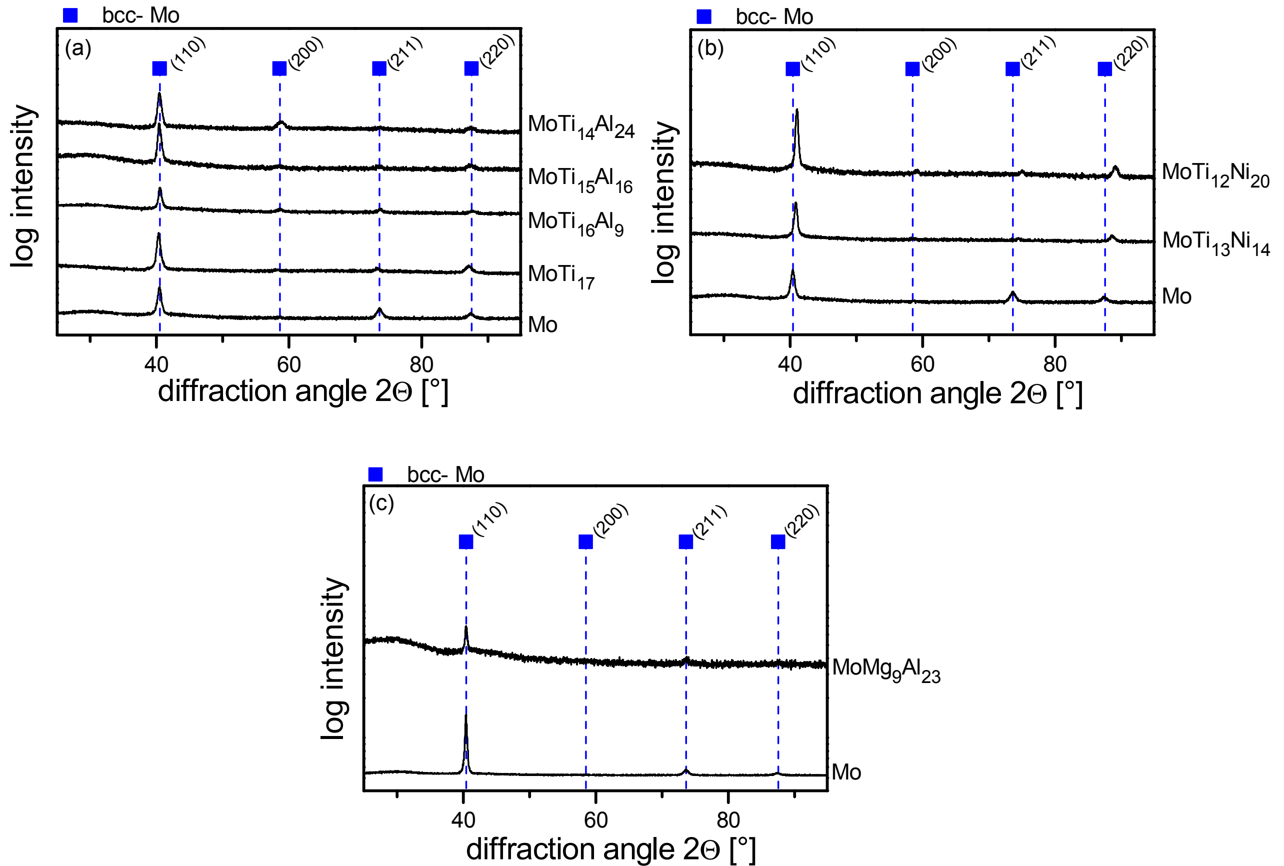

Fig. 1. XRD diffractograms with different compositions in the systems (a) Mo-Ti-Al (b) Mo-Ti-Ni and (c) Mo-Mg-Al compared to an unalloyed Mo film.

The influence of the alloying elements on the wet etching behavior of the films in PAN is shown in Fig. 2. The Mo-Ti-Al films with lower Ti content exhibit superior wet etching ability, compared to the Mo-Ti-Al films with higher Ti content. As mentioned in section 1, pure Ti cannot be dissolved in PAN etching solution. Consequently, the dissolution rate decreases significantly with increasing Ti content. The influence of Al on the wet etching rates of Mo-Ti-Al films was already discussed in section 3.1.2. Fig. 2 also illustrates, that the Mo-Ti-Al films with lower Ti content are generally etched faster than the Mo-Ti-Ni reference films. The wet etching rate of the Mo-Mg-Al films is the highest, exceeding even that of the unalloyed Mo film.

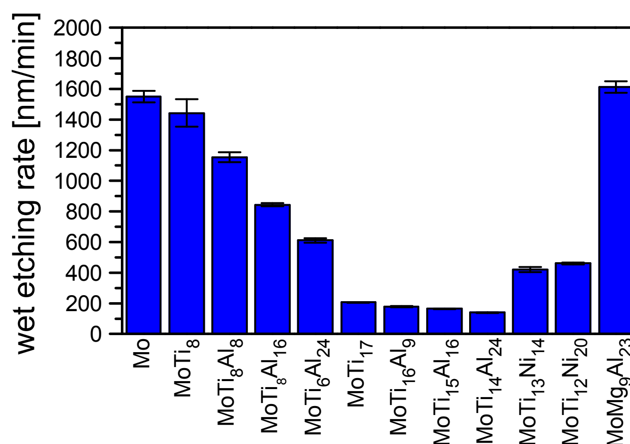

Fig. 2. Wet etching rate of Mo and Mo alloy thin films in PAN.

As outlined in the manuscript, annealing of the as-deposited samples results in the formation of colored oxide films. Fig. 3 contains supplemental photographs of all films after annealing at 330°C for 1h in air. The Mo-Ti-Al film system with lower Ti content was already discussed in detail in section 3.2.2. No colored oxide films are detected by visual inspection of the other ternary Mo alloy films. Similar results are obtained by the reflectance spectra of the films, as shown in Fig. 4. In the as-deposited state, all films exhibit an average reflectance of above 50%, confirming the metallic appearance. However, the reflectivity of the ternary Mo-Ti-Al films with higher Ti content does not change significantly after annealing. The same results are obtained for the Mo-Ti-Ni and Mo-Mg-Al films, indicating the absence of colored oxide films.

Fig. 3. Photographs of the films after annealing at 330°C for 1 h in air.

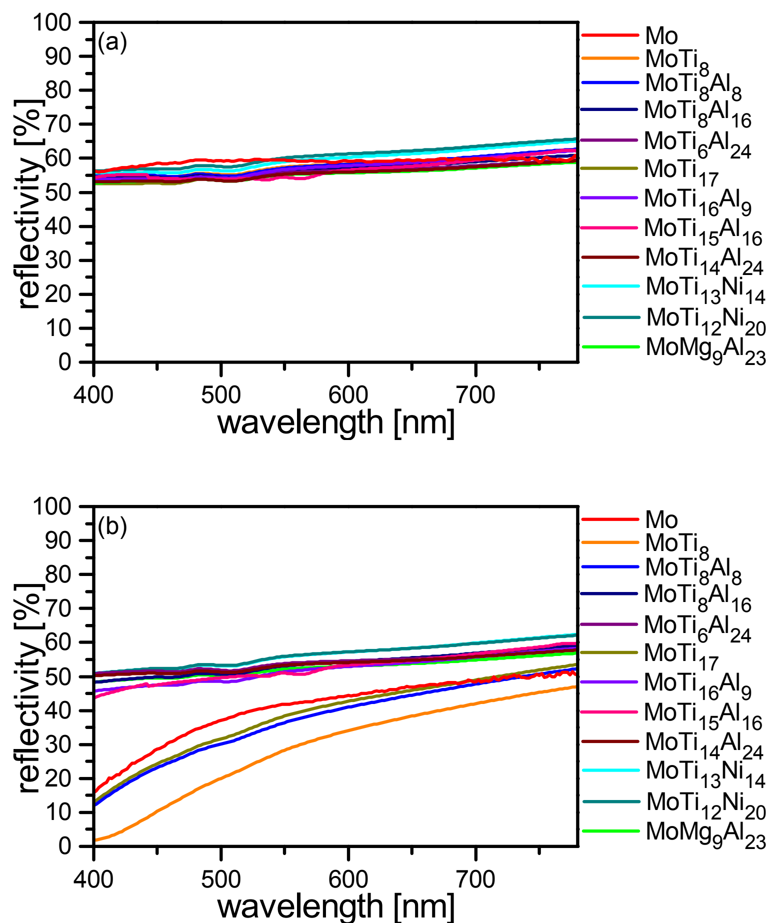

Fig. 4. Optical reflectance spectra (a) before and (b) after annealing of Mo and Mo alloy thin films.

As reported in section 3.2.3, Mo oxides are well suited for characterization by Raman spectroscopy. The Raman spectra of the additional investigated films are shown in Fig. 5. There are no detectable peaks in the spectra of the ternary Mo alloy films. Therefore, it is concluded, that the formation of colored molybdenum oxides is prevented (see section 3.2.3).

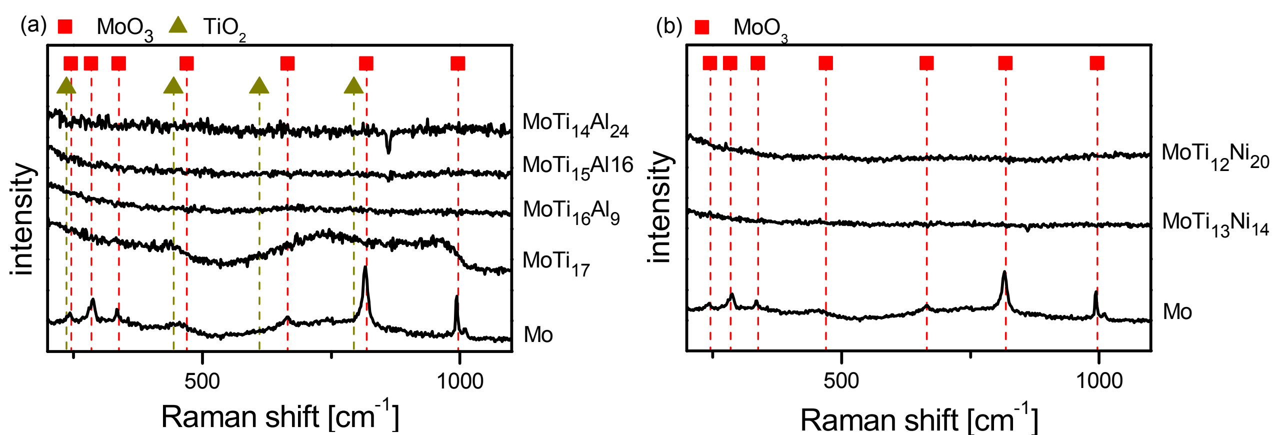

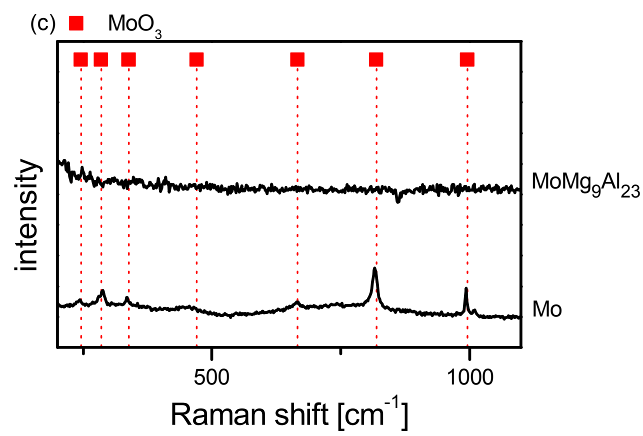

Fig. 5. Raman spectra of (a) Mo-Ti-Al films with higher Ti content (b) Mo-Ti-Ni films and (c) Mo-Mg-Al film compared to an unalloyed Mo film after annealing at 330°C for 1h in air.